Steering the magnetic properties of Ni/NiO/CoO core-shell nanoparticle films: The role of core-shell interface versus interparticle interactions

Alessandro Ponti,[1,*] Anna M. Ferretti,[1] Elena Capetti,[1,†] Maria Chiara Spadaro,[2,3] Giovanni Bertoni,[4] Vincenzo Grillo,[2] Paola Luches,[2] Sergio Valeri,[2,3] and Sergio D'Addato[2,3,‡]

[1]*Laboratorio di Nanotecnologie, Istituto di Scienze e Tecnologie Molecolari, Consiglio Nazionale delle Ricerche, Via G. Fantoli 16/15, 20138 Milano, Italy*

[2]*CNR-NANO, Via G. Campi 213/a, 41125 Modena, Italy*

[3]*Dipartimento FIM, Università di Modena e Reggio Emilia, Via G. Campi 213/a, 41125 Modena, Italy*

[4]*CNR-IMEM, Parco Area delle Scienze 37/a, 43124 Parma, Italy*

(Received 28 April 2017; published 8 August 2017)

Supported core-shell Ni/NiO/CoO nanoparticle (NP) films were obtained by deposition of preformed and mass-selected Ni NPs on a buffer layer of CoO, followed by a top CoO layer. The resulting NPs have core/shell morphology, with a McKay icosahedral Ni core and a partially crystalline CoO shell. X-ray photoelectron spectroscopy evidenced the presence of a thin NiO layer, which was shown to be between the Ni core and the CoO shell by elemental TEM mapping. CoO and NiO shells with different thickness values were obtained, allowing us to investigate the evolution of the magnetic properties of the NP assemblies as a function of the oxide shell thickness. Both exchange-coupling and magnetostatic interactions significantly contribute to the magnetic behavior of Ni/NiO/CoO NP films. After the Ni/NiO/CoO NPs are cooled in a weak magnetic field, they have blocking temperature higher than room temperature because of strong magnetostatic interactions, which support the formation of a spin-glass-like state below ∼250 K. Exchange coupling dominates the magnetic behavior after the NPs are cooled in a strong magnetic field. The exchange bias (EB) is in the 0.17–2.35 kOe range and strongly depends on the CoO thickness (0.4–2.7 nm), showing the onset of the EB at the few-nanometer scale. The switching field distribution showed that the EB opposes the magnetization reversal *from* the direction along the cooling field but it does not significantly ease the opposite process. The EB depends on t_{CoO} only for $t_{NiO} \leqslant 0.5$ nm, but when NiO is 0.7 nm thick it strongly interacts with CoO and a large increase of the EB and coercivity is observed.

DOI: 10.1103/PhysRevMaterials.1.036001

I. INTRODUCTION

Metal/metal oxide (M/MO) core-shell nanoparticles (NPs) are of great interest because of their application in many fields, like magnetic recording, electronics, catalysis, and medical imaging [1,2]. Among the main themes in this research field, control of the synthesis of M/MO NPs is essential for the design of these nanomaterials with desired properties. In the specific case of nanomagnetism, stabilization of NPs at room temperature is a crucial issue, as the superparamagnetic (SPM) limit can hamper the possibility of developing high-density memories consisting of units (bits) as small as a few nanometers in linear size [3–5]. A possible way to stabilize NPs at high temperature exploits the additional torque exerted by the exchange coupling at the interface between a ferromagnetic (FM) and an antiferromagnetic (AFM) material. This effect generally occurs in FM/AFM layered systems, where the Curie temperature of the FM material is higher than the Néel temperature T_N of the AFM material [6,7]. According to a schematic interpretation, if the system is cooled in a magnetic field H starting from $T > T_N$, the interface spins in the AFM material are pinned along a specific direction related to the direction along which the field H aligned the FM spins. After field cooling, when the magnetic field is reversed, the FM spins are subject to a torque exerted by the AFM spins, which contrasts the field-induced rotation, causing a shift of the hysteresis loop in the direction opposite to the cooling field called exchange bias (EB). This shift is quantified by the EB field H_b. Another significant effect occurring in exchange-coupled systems is the hardening of the material with an increase of the coercivity H_c, here defined as the average $(H_c^- + H_c^+)/2$ of the two field values where the magnetization switches from positive to negative values and vice versa during a hysteresis cycle [6,7].

EB can also be observed in core-shell NPs with FM core and AFM shell. Stabilization of core-shell NPs was indeed observed in Co/CoO systems [3,4]. Co NPs were obtained by physical synthesis methods partially oxidized in order to obtain an AF oxide shell and deposited on a substrate. It was found that the EB increased at increasing NP density because of the "recovery" of the AFM properties caused by the neighboring oxide shells coming into contact and providing a more efficient exchange interaction with the FM cores [4]. EB was also observed in other core-shell NP assemblies, either chemically [2,8,9] or physically [10,11] synthesized. In the case of Ni/NiO NPs, different and sometimes contrasting evidence of EB and stabilization was found [12–17], revealing that EB depends strongly on the type of NP preparation, which can affect the

*Author to whom correspondence should be addressed: alessandro.ponti@istm.cnr.it

†Present address: Lens Manufacturing, Luxottica, Corso Torino 7, 10020 Lauriano Po, Italy.

‡Author to whom correspondence should be addressed: sergio.daddato@unimore-it

interface defects and/or dislocations, the crystallinity degree of core and shell, and other factors. In a recent work, different procedures were used for obtaining the oxide shell: exposition to oxygen after deposition, annealing in atmosphere, or reactive deposition of NiO, using a sequential layer deposition procedure [18,19]. The latter method consisted of three steps: (1) an oxide layer was grown on an inert substrate, like a Si wafer with its native oxide, Si/SiO_x; (2) preformed, mass-selected metal NPs were deposited on the ultrathin oxide layer; and (3) an oxide overlayer was grown on the Ni NP assembly. This procedure allows the oxide shell thickness to be varied while maintaining the Ni core diameter fixed. Moreover, non-native oxide shells can be grown. Therefore, optimization of the different parameters governing the EB can be pursued, with the ultimate goal of reaching magnetic stability at room temperature (RT) for NPs with smaller diameter values. In a recent preliminary work, this method was also applied to Ni/CoO NP assemblies [20], with a Ni core diameter of approximately 11 nm. Scanning electron microscopy (SEM) and scanning transmission electron microscopy (STEM) images revealed the core-shell structure on the obtained NPs, and from the analysis of x-ray photoelectron spectroscopy (XPS) data it was found that a thin oxidized Ni shell with thickness of a few atomic layers was formed, presumably at the core-shell interface. This interface layer may play an important role in the exchange coupling between the FM Ni core and the AFM CoO shell.

The exchange coupling at the Ni/CoO interface has not yet been investigated in detail. Simultaneous condensation of evaporated Ni and laser-ablated CoO produced core-shell NP assemblies [21], but the shell around the Ni NPs actually comprised an outer Co_3O_4 layer in addition to a thin intermediate NiO layer. EB was observed up to $T = 45$ K, a temperature close to the Néel temperature of Co_3O_4. Exchange coupling across the Ni/CoO interface was reported for a few thin films. A Ni(30 nm)/CoO(30 nm) bilayer prepared by dc sputtering showed blocking temperature T_B of 295 K, very close to the Néel temperature of CoO, and $H_b = 35$ Oe at 50 K with exchange-coupling energy density $E_A = 0.103 \times 10^{-3}$ J/m^2 [22]. Another multilayer with 2 nm CoO separated from 27–34 nm Ni by 0.4 nm Pt displayed lower $T_B = 175$ K but higher $H_b = 470$–610 Oe at 10 K and $E_A = 0.8 \times 10^{-3}$ J/m^2 [23]. More recently, proximity effects induced by CoO on Ni were investigated in Pd(001)/Ni(001)/CoO(001) multilayers with fixed CoO thickness (3 ML) and Ni thickness up to 25 ML [24]. It was found that a thin NiO layer (about 1 ML) formed at the Ni/CoO interface, leading to an average thickness of the global oxide layer of $\sim$1.3 nm. Such a multilayer has $T_B \approx 250$ K, and magneto-optical Kerr effect experiments at 5 K yielded $H_c \approx 1500$ Oe and $H_b = 100$ Oe, corresponding to $E_A = 0.183 \times 10^{-3}$ J/m^2. The spins in both CoO and NiO are parallel to the layer plane, while the Ni spins are along (001), thus providing perpendicular coupling. The importance of a thin "native" oxide layer between the FM core and the AFM shell has also been demonstrated in an investigation of Co NPs embedded in a NiO matrix, where a thin ($\sim$1 nm) CoO shell was present between the Co cores and the NiO matrix. Despite that the Co cores were a few nanometers in diameter, T_B was found to be higher than 360–400 K. Based on theoretical modeling, the high T_B was attributed to a synergic proximity effect involving a large magnetic anisotropy of CoO and a high Néel temperature of NiO [25].

In this work, a set of thin-film assemblies of Ni/NiO/CoO NPs was produced with different CoO shell thickness using a three-step sequential layer deposition procedure. An investigation of the structure and composition of the core-shell NPs formed the basis to understand the field- and temperature-dependent magnetic properties of the Ni/NiO/CoO NP assemblies and their relationships with the NP structure, in particular with the thickness of the oxide shell. Such a systematic study of the effect of the oxide thickness on the magnetic properties revealed the potentiality and flexibility of the sequential layer deposition method in realizing magnetic nanostructures.

II. EXPERIMENTAL METHODS

The experimental method used to obtain the Ni/NiO/CoO NP assembly has been described in detail in previous papers [26–28]. Three interconnected vacuum chambers (base pressure $p = 8 \times 10^{-9}$ mbar) were used to synthesize the NP, to deposit them on supports, and to analyze *in situ* the obtained assemblies with XPS. The NPs were grown with a gas aggregation nanocluster source equipped with a magnetron sputtering gun (NC200U, Oxford Applied Research, magnetron discharge power $P = 35$ W, Ar flow $f = 50$ sccm) and mass-selected with a quadrupole mass filter (QMF 200, Oxford Applied Research). In these conditions we could obtain Ni NPs with a linear size distribution between 8 and 15 nm and average diameter $\langle d \rangle = 11$ nm, as directly verified by analyzing the SEM images [18,19]. The oxide layers were obtained by reactive deposition of Co with a thermal evaporator in the presence of O_2 [20]. The partial oxygen pressure varied between 5×10^{-8} and 2×10^{-7} mbar, while the power supplied to the evaporator varied between 27 and 30 W. The different conditions for the deposition of the CoO third layer were used to investigate the formation of an interfacial NiO shell between the core and shell (see also the Results section). During the sequential layer deposition steps described in the Introduction, we deposited

(1) A first CoO layer with nominal thickness $t^1_{CoO} = 1$ nm.

(2) A layer of preformed, mass-selected Ni NPs. The amount of deposited Ni, expressed as nominal thickness, was $t^2_{Ni} = 6$ nm. This quantity corresponds to the thickness of a continuous film of bulk Ni, with the same mass as the amount of deposited Ni NPs. It can be estimated that a single layer of close-packed Ni equal spheres with $d = 11$ nm has the same mass as a continuous film with $t^2_{Ni} = 6$ nm. In the case of the samples realized for the STEM and high-resolution TEM (HRTEM) measurements, the amount of Ni NPs was $t^2_{Ni} = 1$ nm, to better resolve the morphology and structure of the single NP.

(3) A CoO overlayer, with variable nominal thickness t^3_{CoO}.

As stated in previous papers [18–20], the first layer of CoO was deposited in order to complete the CoO shells around the Ni NPs (also between the substrate and the deposited NPs). The deposition rate of the different materials was monitored with a quartz microbalance. Different values for the power supplied to the Co evaporator were used in order to change the crucible Co temperature and the evaporation rate. In this

way, it was possible to obtain different thickness values for the interfacial NiO layers between the Ni core and CoO external shell, which were found during previous experiments [20,21]. The values of the supplied power ranged between 89.3 and 130 W, corresponding to evaporation temperatures between 1450 and 1600 K, as measured with a thermocouple positioned close to the Co crucible. Si with its native oxide (Si/SiO_x) wafers were used for samples to be analyzed with XPS, SEM, and superconducting quantum interference device (SQUID) measurements, while carbon-coated copper and lacey grids were employed for STEM and HRTEM measurements. *In situ* XPS analysis was performed after each deposition step by making use of an Al-Mg twin anode x-ray source (XR50, Specs), generating Mg $K\alpha$ photons ($h\nu = 1253.6$ eV), and an electron hemispherical analyzer (Phoibos 150, Specs). The amount of the deposited material was estimated also from the intensity of Ni, Co, and Si $2p$ core-level XPS spectra. The STEM and HRTEM experiments were performed using a JEOL JEM-2200FS microscope equipped with a Schottky field-emission gun working at 200 keV. The instrument has an objective lens spherical aberration coefficient of 0.5 mm, permitting a point-to-point resolution of 0.19 nm. Electron energy loss spectroscopy (EELS) measurements were performed in STEM mode, with a spot size of 0.5 nm, with the in-column filter (Ω type) in spectroscopy mode. Image and data analysis were carried out with STEM-CELL and EELSMODEL software [29,30].

Magnetization measurements were carried out by a Quantum Design MPMS XL-5 SQUID magnetometer. Field-cooled (FC) and zero-field-cooled (ZFC) magnetization curves were recorded in the 5–400 K range as follows. The sample was heated from RT to 400 K in zero field and then cooled to 5 K in zero field. The ZFC magnetization was recorded on heating using a measuring field $H_{meas} = 100$ Oe. Next, the FC magnetization was measured ($H_{meas} = 100$ Oe) while cooling the sample from 400 K to 5 K under field $H_{cool} = 100$ Oe. The thermal behavior of the thermoremanent magnetization (TRM) was recorded as follows. After being heated to 400 K in zero field, the sample was subjected to a cooling field H_{cool} (100, 1000, or 10 000 Oe) and cooled to 5 K. After switching off the field, the remanent magnetization was recorded while heating the sample from 5 to 400 K. Magnetization isotherms (hysteresis loops) were recorded between +50 kOe and –50 kOe at 300 K. Low-temperature (5-K) magnetization isotherms were recorded in both ZFC and FC modes after heating the sample to 400 K in zero field; in FC mode the sample was cooled to 5 K with $H_{cool} = +50$ kOe. dc demagnetization (DCD) curves were recorded as follows. The sample was heated to 400 K and cooled to 5 K in zero field, and then a positive saturating (+50 kOe) field was applied and removed; afterwards a series of increasingly negative fields (up to –20 kOe) was applied and removed, and the remanent magnetization was recorded. To investigate the exchange coupling, the DCD remanence was also measured after cooling in either positive or negative field (+50 or –50 kOe); in both cases the saturating field was positive and the demagnetization field negative. All data were corrected for support diamagnetism [31,32] and scaled to the nominal deposited nickel mass.

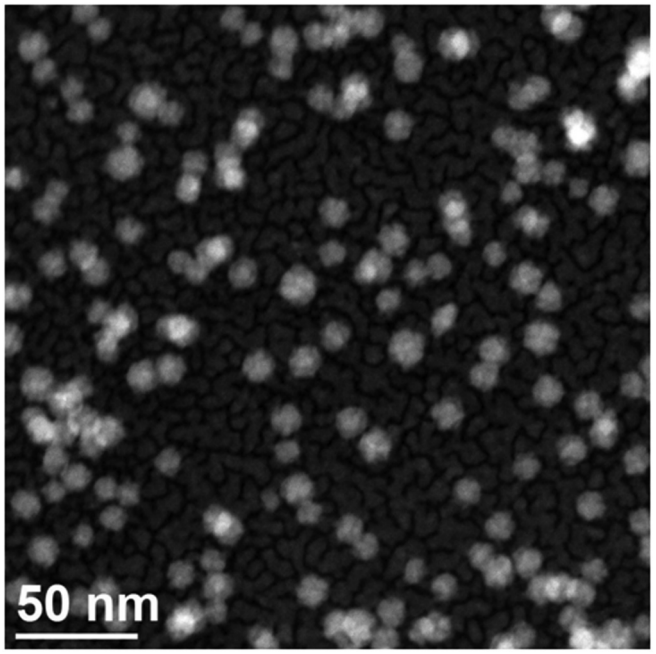

FIG. 1. STEM image of Ni/NiO/CoO NPs grown with sequential layer deposition, where $t^1_{CoO} = 1$ nm, $t^2_{Ni} = 1$ nm, and $t^3_{CoO} = 2$ nm.

III. MORPHOLOGY AND STRUCTURE

Figure 1 displays STEM images of a Ni/NiO/CoO NP film obtained with the sequential layer deposition. The NPs have a shape compatible with the McKay icosahedron [33], as previously observed on bare Ni, FePt, Cu, and other fcc metal NPs and nanoalloys [27,34–37]. The icosahedron is composed of fcc Ni tetrahedral crystallites with slightly distorted (111) facets. This structure is due to multitwinning occurring during the Ni cluster growth in the gas aggregation source, caused by cluster freezing in a metastable state [38,39]. Some small irregularities are present on the NP surfaces due to the presence of CoO islands grown after the deposition of the overlayer. For this sample, the nominal thicknesses of the three layers were $t^1_{CoO} = 1$ nm, $t^2_{Ni} = 1$ nm, and $t^3_{CoO} = 2$ nm, respectively, as estimated by the evaporation rate with the quartz microbalance. In addition, the NPs lie on an irregular surface due to the presence of CoO deposited on the substrate during steps (1) and (3) of the sequential deposition, with the morphology of a percolated film.

The core-shell structure of the obtained NPs is clear in the HRTEM images reported in Fig. 2. The lattice fringes of the Ni core and of the oxide shells are clearly visible. The Ni core structure is compatible with the (111) facets of the McKay icosahedron. In Fig. 2(b) the HRTEM image of a thinner sample is shown ($t^1_{CoO} = 1$ nm, $t^2_{Ni} = 1$ nm, and $t^3_{CoO} = 0.5$ nm). From this image it was possible to evaluate the CoO layer growth direction on the Ni NP surface. A sharp core-shell interface is clearly visible, and it was possible to investigate the lattice fringe periodicity: in the core it was found $d = 0.246$ nm, corresponding to Ni (111) planes, while in the CoO shell indicated by the arrow the lattice fringe periodicity was measured as $d = 0.218$ nm, corresponding to CoO (002)

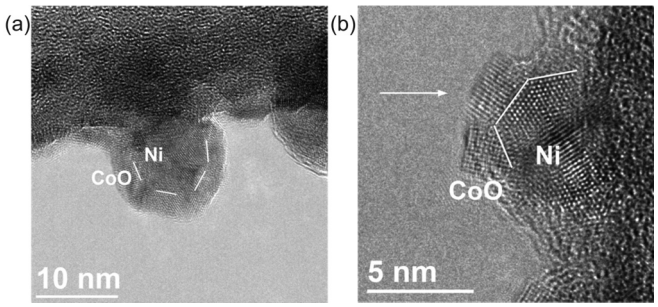

FIG. 2. (a) HRTEM image of a Ni/NiO/CoO NP ($t^1_{CoO} = 1$ nm, $t^2_{Ni} = 1$ nm, and $t^3_{CoO} = 2$ nm) protruding from the lacey carbon support. The white polygonal line outlines the Ni core within the oxide shell. (b) HRTEM image of Ni/NiO/CoO NP ($t^1_{CoO} = 1$ nm, $t^2_{Ni} = 1$ nm, and $t^3_{CoO} = 0.5$ nm) showing the Ni/CoO NP interface. The white arrow indicates a CoO island with a well-defined crystal structure and lattice orientation.

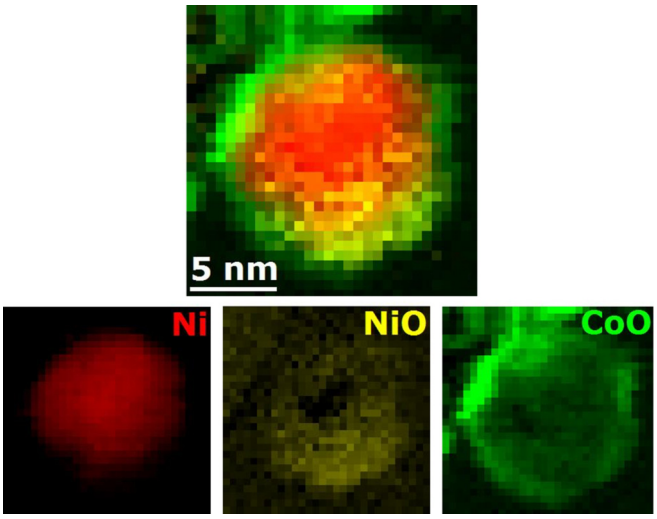

FIG. 3. Results of the fitting of the EELS map for metallic Ni (red), NiO (yellow), and CoO (green) components.

planes. The average thickness of the CoO shell is 2.5 nm for the NP in Fig. 2(a) and 0.9 nm for the NP in Fig. 2(b), in good agreement with the nominal values.

SEM images of Ni/NiO/CoO NPs grown on Si/SiO_x have been previously reported [20]; at increasing coverage of the CoO overlayer, the islands cover completely the Ni NP cores and extend over neighboring NPs, forming nanostructures of cubic shape with size between 15 and 50 nm at the highest overlayer thickness studied ($t^3_{CoO} = 6$ nm). XPS analysis confirmed that the oxide shell consisted mainly of CoO (at variance with previous experiments [21], where the NPs prepared with a similar technique had an oxide shell composed of Co_3O_4 and Co suboxides) and showed also that an interfacial NiO shell was formed during the deposition of the CoO overlayer. The data also showed that NiO was formed during the deposition of the CoO overlayer. Oxidation of the external layers of the Ni cores, as previously reported [20,21], can be ascribed to a slightly higher electronegativity value of Ni (1.91 Pauling) with respect to Co (1.88 Pauling). Therefore, Ni external layers are oxidized during the reactive deposition of CoO, as O_2 gas is present during this procedure and can react with Ni. In order to estimate the amount of oxidized Ni, a model was assumed in which an interfacial NiO layer is formed between the Ni core and the CoO shell. HRTEM images did not show a clear evidence of the formation of this interfacial shell, probably because of the similar lattice parameter values ($a = 0.418$ nm for NiO and 0.426 nm for CoO) and crystal structure (rocksalt for both materials). The presence of the oxide shell was demonstrated by EELS in STEM mode on the sample with $t^3_{CoO} = 2$ nm by acquiring a spectrum image (or EELS map). The spectra were fitted using a power-law background combined with three reference spectra, a Ni-$L_{2,3}$ from metallic Ni, a Ni-$L_{2,3}$ from NiO, and a Co-$L_{2,3}$ edge from CoO. The results are shown in Fig. 3. The nanoparticle core is composed by metallic Ni (red) surrounded by a thin NiO shell (yellow) and an outer CoO shell (green).

The resolution of the image in Fig. 3 is limited by the fact that an EELS spectrum was acquired at each point. For this reason, the thickness of the NiO shell was evaluated by the analysis of the Ni and Co $2p$ XPS line intensities with a method developed by Shard [40]. The obtained value depends on the choice of the parameters governing the CoO growth, and it varies between $t_{NiO} = 0.17$ and $t_{NiO} = 0.67$ nm, corresponding to *ca.* 0.25–1.5 NiO atomic cells. With the same method, it was possible to obtain the thickness of the CoO shell surrounding the Ni/NiO NP core, t_{CoO}. The thicknesses of the NiO and CoO shells are reported in Table I together with the corresponding nominal thickness of the CoO overlayer, t^3_{CoO}. It must be stressed that t^3_{CoO} is a quantity expressing the amount of CoO deposited during step 3 of the NP growth method summarized in the previous section (growth of the third layer) and estimated by the evaporation rate measured by the quartz microbalance, while t_{CoO} is an estimate of the CoO shell average thickness in Ni/NiO/CoO NPs as obtained by analysis of the XPS Co $2p$ components [38]. The different values of t^3_{CoO} are due to the different conditions used for CoO deposition (evaporator power and deposition time) in order to investigate the effect of the interfacial NiO shell on the magnetic properties of the NP films. The model used is indeed an approximation and the NiO and CoO thickness values are assumed to be accurate only within ±5 Å, as confirmed also by the comparison with

TABLE I. Nominal thickness of the third (CoO) layer estimated with a quartz microbalance (t^3_{CoO}) compared to the thickness of the intermediate NiO (t_{NiO}) and outer CoO (t_{CoO}) layers as determined from XPS data. We note that while the values reported for the CoO and NiO thickness have a precision of the order of 0.01 nm, their accuracy is certainly limited by the approximations included in the model (see text).

Sample	t^3_{CoO} (nm)	t_{CoO} (nm)	t_{NiO} (nm)
A	0.5	0.43	0.30
B_1	1.0	1.01	0.47
B_2	2.0	1.00	0.50
B_3	1.0	1.02	0.67
C	1.5	1.21	0.15
D	1	2.29	0.29
E	2	2.66	0.17

the values of the CoO thickness obtained by the analysis of Fig. 2.

A more realistic picture of the NPs includes an intermediate oxide region between the Ni core and the pure CoO shell region with a mixture of Co and Ni oxides. The mutual polarization of Co and Ni ions can have non-negligible consequences on the magnetic properties of the system, as observed in [25] and [41].

IV. MAGNETIC PROPERTIES

fcc nickel is a ferromagnetic metal with saturation magnetization $M_s(0\,\mathrm{K}) = 58.57\,\mathrm{emu/g}$ [42] and low magnetocrystalline anisotropy ($K_1 = -5.7 \times 10^3\,\mathrm{J/m^3}$ and $K_2 = -2.3 \times 10^3\,\mathrm{J/m^3}$ at 296 K [43]) with easy axis along ⟨111⟩. The characteristic diameter for both coherent rotation and the single-domain state of Ni NPs is close to 50 nm [44]. The superparamagnetic (SPM) blocking diameter for spherical ideal Ni NPs (i.e., noninteracting NPs free of surface effects) can be estimated at 70 nm at 300 K and 8 nm at 4 K, taking into account the strong temperature dependence of the cubic anisotropy constants of Ni [45]. Thus ideal Ni NPs with the same size as those in the investigated films (diameter ∼11 nm) [19,20] would be single-domain NPs with coherently rotating magnetization and would display SPM behavior at RT and blocked behavior at $T = 5\,\mathrm{K}$. Their estimated blocking temperature T_B is ∼20 K. The Ni NPs in our films are (purposely) far from being ideal, since (i) a thin oxide layer coating the Ni NPs gives rise to exchange coupling at the interface, and (ii) short NP-NP distances make magnetostatic interparticle interactions significant. (Note that we use the general term "magnetostatic" instead of "dipolar" interaction, since the interaction between magnetized particles separated by distances comparable to their size may contain terms of higher order than the dipolar term.) We assume that the Ni NPs maintain the single-domain state and the coherent magnetization rotation mode and focus our investigation on the changes of the Ni magnetization behavior due to exchange coupling, while bearing in mind the presence of inter-NP interactions.

The Ni NPs are coated by a composite layer oxide. Close to the Ni surface, a thin (0.2–0.7 nm) intermediate NiO layer is present. NiO is a type-II AFM oxide with high Néel temperature (bulk 525 K) and very low magnetocrystalline anisotropy (bulk $K_1 = -500\,\mathrm{J/m^3}$) [44]. The top coating is a layer of CoO with thickness ranging from 0.4 to 2.7 nm. CoO is an AFM oxide with a debated magnetic structure, probably displaying a mixture of type-I and type-II ordering [45]. At variance with NiO, CoO has low Néel temperature (bulk 291 K) and very high magnetocrystalline anisotropy (bulk $K_1 \approx 10^7\,\mathrm{J/m^3}$) [46,47].

A. ZFC/FC and TRM

The zero-field-cooled (M_{ZFC}) and field-cooled (M_{FC}, $H_{cool} = 100\,\mathrm{Oe}$) magnetization was recorded between 5 and 400 K. All samples gave similar results, which are collected in Table II and exemplified in Figs. 4(a)–4(d). M_{FC} increases down to $T \approx 250\,\mathrm{K}$ and then reaches a minimum at low temperature, indicating the formation of a spin-glass-like state. M_{ZFC} vanishes at low temperature and displays a steep increase between 150 and 300 K, showing that an anisotropy barrier is overcome in this temperature range. M_{ZFC} is maximum at $T_{max} = 270$–330 K, indicating a blocking temperature comparable to RT. This behavior can be better appreciated by calculating the derivative $-d(M_{FC}-M_{ZFC})/dT$, which is an approximate representation of the distribution of the barriers to magnetization reversal (Fig. 4). The most probable barrier, which is another estimate of T_B, corresponds to the temperature T_{der}, where the derivative is maximum. In our NP assemblies, T_{der} lies in the 220–250 K range (Table II). Note that sample A displays an additional peak at 30 K in the $-d(M_{FC}-M_{ZFC})/dT$ curve.

In addition to the ZFC/FC magnetization, the low-field behavior of the assemblies of Ni/NiO/CoO NPs was investigated by monitoring the thermal behavior of the thermoremanent magnetization created by cooling the sample from 400 to 5 K in a magnetic field. TRM is complementary to ZFC/FC data, since M_{TRM} is free from reversible magnetization. All samples gave similar results (Table II), and selected TRMs are shown in Figs. 4(e)–4(h). Before discussing the results, it should be clarified why the TRM becomes negative at high temperature. After some debate, it was demonstrated that such effects are artifacts arising from the hysteresis of the magnet superconducting coils [48]. We confirmed this conclusion in the TRM case and were able to show that the magnetic parameters calculated are not affected by these artifacts [49]. TRM was recorded after application of different cooling fields (100 and 10000 Oe). With reference to the 300-K magnetization isotherm (see below), these cooling fields are able to magnetize the Ni/NiO/CoO NPs up to 30% and 100% of the RT saturation magnetization. The low-temperature TRM

TABLE II. Estimates of the blocking temperature from ZFC/FC magnetization and TRM of thin-film assemblies of Ni/NiO/CoO NPs.[a]

	ZFC/FC		TRM $H_{cool} = 10^2$ Oe	TRM $H_{cool} = 10^4$ Oe
Sample	T_{max} (K)	T_{der} (K)	T_{der} (K)	T_{der} (K)
A	330	30, 210	30, 200	
B_1	330	250	260	15, 260
B_2	270	220	250	15, 240
B_3	290	240	260	260
C	300	220	240	10, 230
D	340	240	250	25, 230
E	330	230	230	15, 170

[a]The estimated uncertainty is ±5 K.

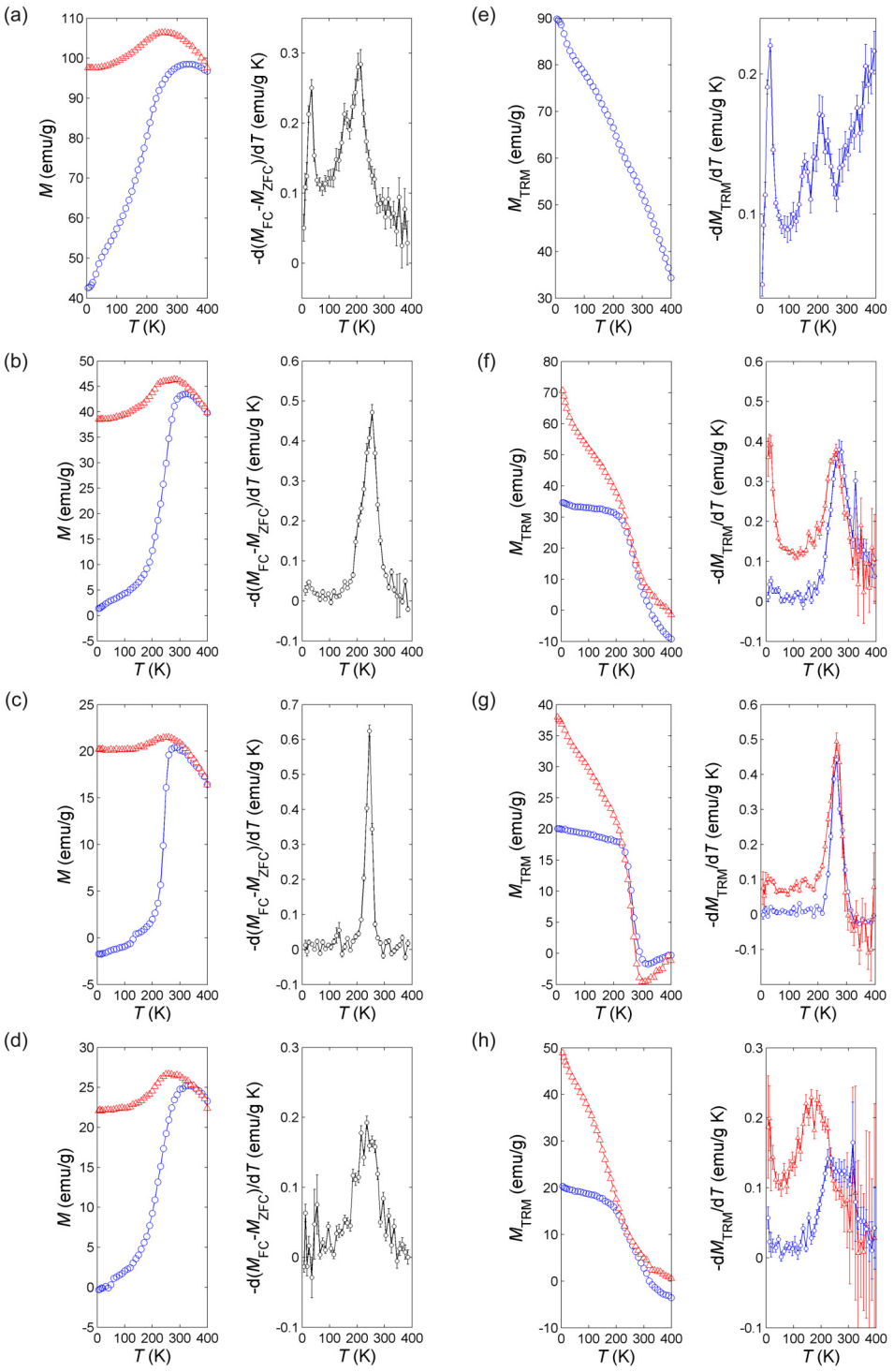

FIG. 4. ZFC/FC and thermoremanent (TRM) magnetization of samples A (a, e), B_1 (b, f), B_3 (c, g), and E (d, f). In each panel the magnetization is plotted in the left graph and the corresponding derivative is plotted in the right graph. The derivative plot also shows error bars. In the left column panel M_{ZFC} (blue circles) and M_{FC} (red triangles) are portrayed along with the derivative $-d(M_{FC}-M_{ZFC})/dT$ (black). In the right column, M_{TRM} is plotted next to the derivative $-dM_{TRM}/dT$ (blue circles: $H_{cool} = 100$ Oe; red triangles: $H_{cool} = 10$ kOe).

is larger for stronger cooling fields, as expected, and slowly decreases upon heating, as the NPs become able to overcome the anisotropy barrier. The TRM measured after cooling in an unequal field become similar close to 250 K and then display a steep decrease. Again, such a decrease is better analyzed by taking the derivative $-dM_{TRM}/dT$ and locating its maximum (Table II and Fig. 4). When $H_{cool} = 100$ Oe, T_{der}(TRM) lies in the 230–260 K range. In general, this $-dM_{TRM}/dT$ peak is broader and asymmetric (toward higher temperatures) for samples with a thicker CoO shell; sample B_3 is an exception, having a narrow symmetric peak despite the intermediate thickness of the CoO layer and total oxide layer. An additional

peak in $-dM_{TRM}/dT$, located at 30 K, is observed for sample A. When $H_{cool} = 10$ kOe, such a low-temperature peak is observed for all samples (15–20 K) and the peak at higher temperature is shifted and broadened towards low temperature.

The ZFC/FC and TRM data allow us to discuss the low-field magnetism of the assemblies of core-shell Ni/NiO/CoO NPs. The observed behavior is different from that expected for ideal 11-nm Ni NPs, and these differences could in principle be attributed to (i) surface effects, (ii) intra-NP exchange coupling at the metal/oxide interface, and (iii) inter-NP magnetostatic interactions. The main change from ideal behavior is the blocking temperature T_B, much higher than the calculated value (∼20 K), and the $T_B = 25$ K observed in 15 nm fcc Ni NPs [50]. The T_B of our Ni/NiO/CoO NPs, as calculated from ZFC/FC and TRM data under weak $H_{cool} = 100$ Oe, is almost independent of the thickness of the NiO and CoO shells. Since in systems where magnetization blocking is due to exchange coupling, T_B strongly depends on $t_{CoO} < 10$ nm [46], the observed T_B cannot be primarily caused by exchange coupling. The T_B of our Ni/NiO/CoO NPs values are not far from the $T_B = 210$ K reported for a thin-film assembly of 10-nm fcc Ni NPs, which was shown to be a random magnet with field-dependent relaxation dominated by magnetostatic interactions below T_B [51]. The blocking behavior is field-dependent also for our Ni/NiO/CoO samples, as demonstrated by comparing the TRMs after cooling in 100-Oe or 10-kOe field. Therefore, we can conclude that T_B is mainly determined by inter-NP magnetostatic interaction.

Our ZFC/FC and TRM data can be interpreted in the framework of a model put forward for core-shell NPs [52]. The magnetic barriers corresponding to the low-temperature peak in the $-dM/dT$ derivatives (10–30 K) can be attributed to interactions within individual Ni NPs, typically surface effects, and are more apparent when a large cooling field hinders the formation of the spin-glass-like state supported by inter-NP magnetostatic interactions. The large magnetization relaxation occurring in the range 220–260 K can be interpreted as the overcoming of the barriers due to magnetostatic interactions. This conclusion is further supported by the following considerations: (i) T_B for the present Ni/NiO/CoO NP assemblies and the previously investigated Ni/NiO assemblies [19], having equal size and density of Ni cores, are very close; (ii) T_B (and the steep increase in M_{ZFC}) occurs at the temperature where M_{FC} decreases because of the formation of a spin-glass-like state; (iii) preliminary experiments show that M_{ZFC}, M_{FC}, and TRM are different when measured parallel or perpendicular to the substrate.

However, a contribution of the FM/AFM exchange coupling to the mainly magnetostatic barriers cannot be excluded. The estimated T_B are comparable to those reported for CoO layers (200–290 K) when the blocking is due to exchange coupling [53] and with the $T_B = 250$ K recently measured in Ni(001)/CoO(001) thin films [24]. Moreover, the temperature range in which the magnetization from uncompensated spins in a polycrystalline CoO layer vanishes [54] is comparable to the T_B range displayed by our Ni/NiO/CoO NP films. Indeed, a larger intra-NP anisotropy caused by the FM/AFM exchange coupling would increase the blocking temperature by preventing SPM to weaken the magnetostatic interaction. For instance, when the spins undergo fast relaxation, the dipole-dipole interaction enters the Keesom regime, where it has shorter range (r^{-6}) than for nonrelaxing spins (r^{-3}) [55]. In conclusion, a complex interplay of magnetostatic and exchange-coupling interactions might be responsible for the magnetization unblocking at T_B. Some light on this issue could be shed by the investigation of samples differing in the NP areal density, e.g., on decreasing the areal density from N_1 to N_2, the average interparticle distance increases by the factor $(N_1/N_2)^{1/2}$, thus weakening the inter-NP interactions while leaving surface and exchange-coupling effects unaltered.

B. Isothermal magnetization

The magnetization isotherms $M(H)$ recorded at 300 K are closed magnetization loops, indicating the complete magnetic reversibility of Ni/NiO/CoO NP assemblies (SPM regime) at this temperature. Magnetic saturation is reached at $H \cong \pm 1$ kOe [49]. Open hysteresis loops symmetrically located with respect to $H = 0$ and with coercivity $H_c < 1$ kOe are observed at 5 K when $M(H)$ is recorded after zero-field cooling [49]. Saturation and reversibility are reached at rather high field $H \cong \pm 10$ kOe, supporting the presence of significant inter-NP magnetostatic interactions. These data show that the Ni/NiO/CoO NPs are in the blocked regime at 5 K and significantly interact by magnetostatic interactions when the magnetic behavior is prevented to show EB effects by cooling in zero field.

The EB effects can be investigated by recording the isothermal magnetization at 5 K after cooling in strong field ($H_{cool} = +50$ kOe), so that EB is established and shows up as a nonvanishing bias field H_b and increased coercivity H_c. Field cooling also hinders the formation of a spin-glass-like state at low temperature. Under FC, all samples display open hysteresis loops with substantial shifts towards negative H. The magnetic parameters are reported in Table III, and selected isotherms are displayed in Fig. 5.

The general trend is that both coercivity H_c and EB field H_b are larger for thicker CoO shells: H_b ranges from 0.17 kOe for $t_{CoO} = 0.43$ nm to about 2 kOe for the samples with $t_{CoO} > 2$ nm, and H_c ranges from 0.56 kOe for $t_{CoO} = 0.43$ nm to more than 2 kOe for the samples with $t_{CoO} > 2$. The coercivity of the remanence, here calculated by the ΔM method [56], is an approximation to the median value of the coercivity of individual NPs, i.e., the median of the switching field distribution (SFD) [57]. Because of the unidirectional asymmetry induced by field cooling, we must distinguish between the descending (H_{cr}^-) and ascending branches (H_{cr}^+). H_{cr}^- is related to reversing the magnetization of a NP *from* the preferred direction set by the cooling field, and vice versa for H_{cr}^+. The latter slowly increases from 0.44 kOe for $t_{CoO} = 0.43$ nm to about 1 kOe for the sample with a thick CoO layer, whereas H_{cr}^- ranges from –0.82 kOe for $t_{CoO} = 0.43$ nm to nearly 6 kOe for the samples with $t_{CoO} > 2$ nm. This different behavior suggests that the main effect of the AFM/FM exchange coupling is to dramatically increase the coercivity of individual NPs when their magnetization is reversed *from* the cooling direction. More details about the modification of the SFD brought about by exchange coupling can be found in the next section.

TABLE III. Magnetic parameters related to the isothermal magnetization of Ni/NiO/CoO NP films.

Sample	H_b (kOe)	H_c (kOe)	H_{cr}^- (kOe)[a]	H_{cr}^+ (kOe)[b]	M_r/M_s (%)[c]	M_r/M_s EB corr (%)[d]
A	0.17	0.56	−0.82	0.44	83	74
B_1	0.83	1.19	−2.38	0.49	86	65
B_2	0.71	1.24	−2.06	0.73	85	63
B_3	2.35	3.15	−5.76	1.25	90	67
C	1.39	1.81	−3.84	0.82	90	65
D	2.15	2.76	−5.47	1.01	102	71
E	1.91	2.19	−5.82	0.74	91	57

[a]Remanent coercivity measured on the descending branch of the ΔM curve (positive H_{cool}).
[b]Remanent coercivity measured on the ascending branch of the ΔM curve (positive H_{cool}).
[c]Squareness ratio calculated using the usual definition of remanence $M(H = 0)$.
[d]Squareness ratio calculated using the EB-corrected remanence $M(H = -H_b)$ [49].

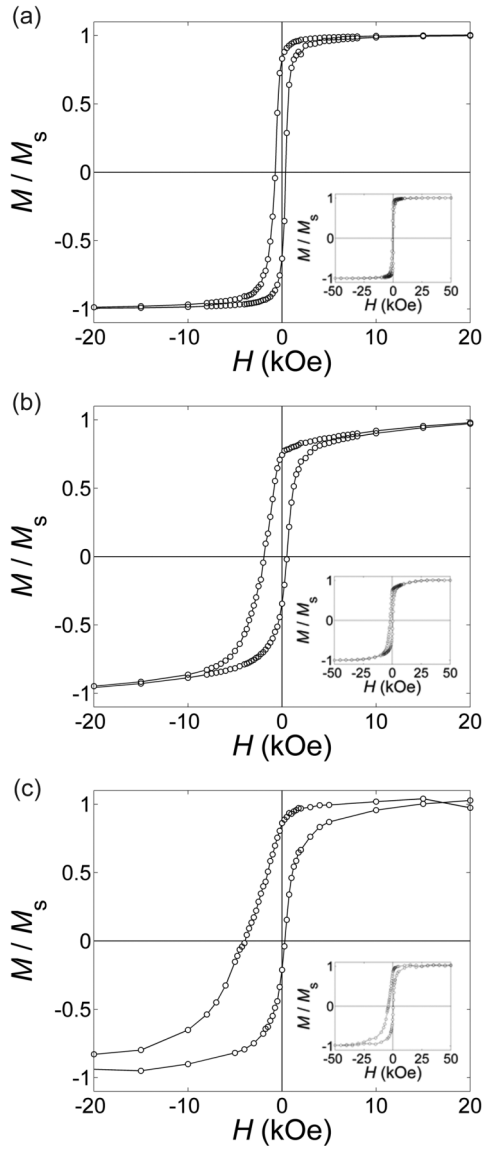

FIG. 5. FC magnetization isotherm (5 K) of samples A (a), B_2 (b), and E (c). The insets portray the full ±50-kOe field interval of the FC isotherms.

The EB field of our Ni/NiO/CoO core-shell NPs compares well with literature values. Though it is lower than that observed for 4-nm Co NPs in a CoO matrix ($H_b = 7.4$ Oe) [3] where smaller FM NPs are embedded in a thick AFM matrix, H_b is comparable to that of coevaporated Co-CoO films (2.8 kOe) [58] and larger than $H_b \approx 1.1$ kOe measured in oxygen-implanted 30-nm Co films [59]. Our Ni/NiO/CoO NP assemblies have exchange-coupling energy density E_A ranging from 0.07 to 0.27×10^{-3} J/m^2, comparable to those ($0.03–0.12 \times 10^{-3}$ J/m^2) observed in thin-film Permalloy-CoO systems with a thicker polycrystalline CoO layer (1.6–10 nm) [54]. The $E_A = 0.183 \times 10^{-3}$ J/m^2 reported for a Ni(001)/CoO(001) multilayer with $t_{NiO} + t_{CoO} = 1.3$ nm [24] can be compared with $E_A \approx 0.13 \times 10^{-3}$ J/m^2 displayed by samples B_2 and B_3 having $t_{NiO} + t_{CoO} = 1.5$ nm. The Ni/CoO exchange coupling is much more effective than the Ni/NiO coupling, as can be appreciated by comparing these data with those observed for similar thin-film assemblies of Ni/NiO core-shell NP [19]. For instance, sample A with a total oxide thickness of 0.73 nm ($t_{NiO} = 0.30$ nm, $t_{CoO} = 0.43$ nm) has H_b comparable to that of Ni/NiO NPs with $t_{NiO} \approx 2$ nm (the Ni cores have the same size).

Inspection of Table III shows that the EB field and coercivity of sample B_3 are anomalously large: they are the largest among all samples despite the intermediate thickness of the CoO layer and total oxide layer. We will later discuss the peculiarities of sample B_3. For the present, we just recall that B_3, which has the thickest NiO layer, also displayed anomalous ZFC/FC and TRM data.

In the FC hysteresis loops of exchange-biased systems, the remanence M_r (and therefore the squareness ratio M_r/M_s) can be computed in different ways (see [49] for a graphical definition of remanences). The squareness ratio M_r/M_s calculated using the usual remanence $M(H = 0)$ is 85%–100%. However, when one is interested in the energy product $(BH)_{max}$, which is proportional to the area enclosed by the loop and not affected by the loop shift, M_r/M_s calculated using the EB-corrected remanence is a more informative index, since it is depurated from the effects of the loop shift (H_b). The EB-corrected M_r/M_s is approximately 60%–70%, larger than the 40%–50% value observed in the ZFC loops. Thus, exchange coupling at the AFM/FM interface increased the energy product of the NP assembly, as already observed for ball-milled $SmCo_5$/NiO [60].

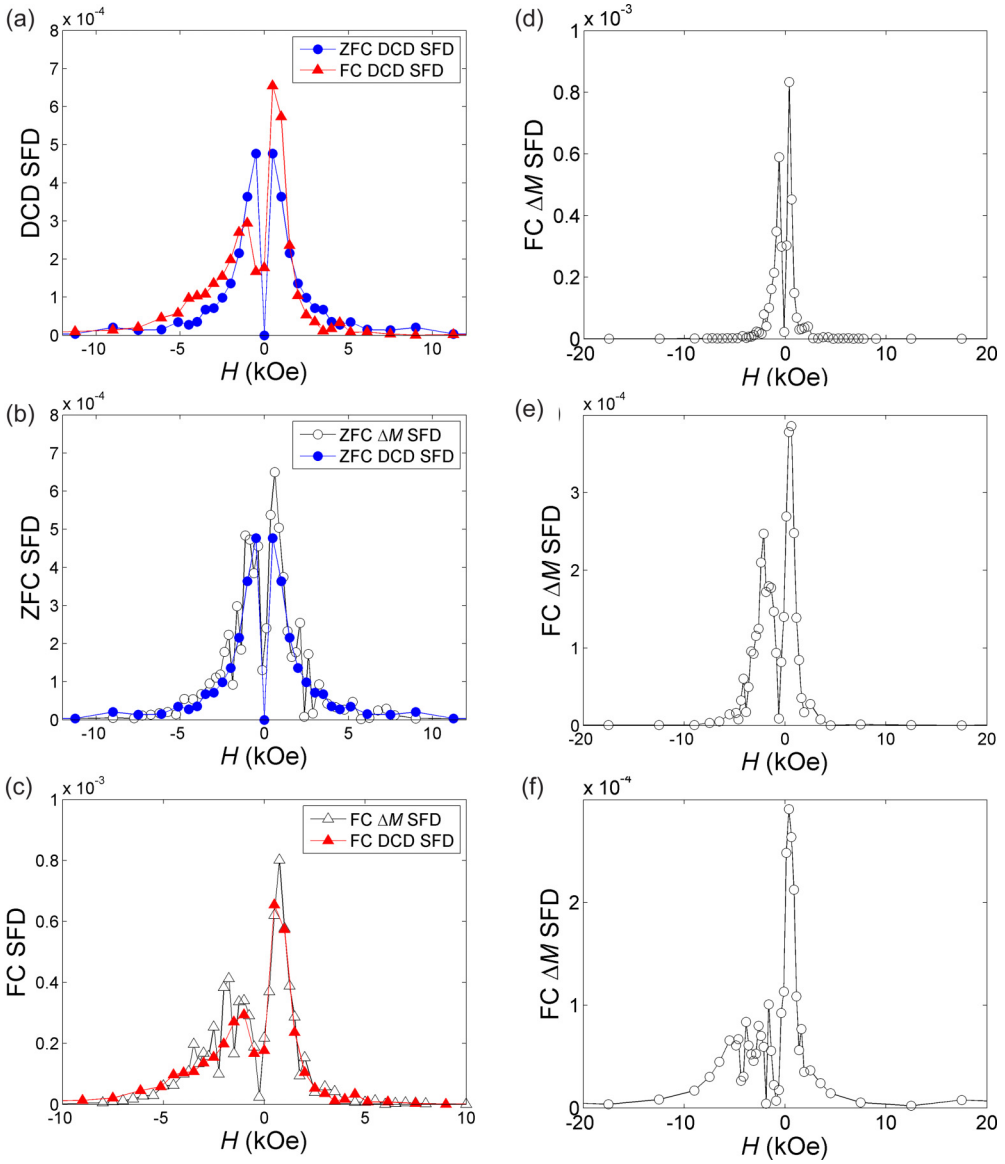

FIG. 6. Switching field distribution (SFD) of core-shell Ni/NiO/CoO NPs. Left column: SFD of sample B_2 from DCD and ΔM data. (a) DCD SFD ($|dM_r^{DCD}/dH|$) of sample B_2 for the ZFC (blue circles) and FC (red triangles) modes. (b) Comparison of DCD ($|dM_r^{DCD}/dH|$) and ΔM ($|d\Delta M/dH|$) SFD from data collected in ZFC mode. Blue circles: DCD; black open circles: ΔM. (c) Comparison of DCD ($|dM_r^{DCD}/dH|$) and ΔM ($|d\Delta M/dH|$) SFD from data collected in FC mode. Red triangles: DCD; black open triangles: ΔM. Right column, approximate SFD from ΔM data ($|d\Delta M/dH|$) of samples A (d), B_1 (e), and E (f). All SFDs have been normalized so that $\int_{-\infty}^{+\infty} SFD(H)\, dH = 1$.

C. dc demagnetization and ΔM

More insight into the effect of EB on the magnetism of NPs can be gained by investigating the distribution of the NP switching field (SFD), i.e., the field at which the magnetization of single NPs irreversibly changes direction. In the present case of assemblies of Ni/NiO/CoO NPs, the concept of SF of individual particles is not fully appropriate since the NPs are coupled by the magnetostatic interaction. However, considering that cooling in strong fields hinders the formation of a spin-glass-like state supported by magnetostatic interactions, the SFD can give some insight into the magnetism of Ni/NiO/CoO NPs, provided it is measured after FC. The DCD remanence M_r^{DCD} represents irreversible magnetization changes since it is measured at zero field and thus the absolute value of the derivative of the DCD remanence with respect to the field, $|dM_r^{DCD}(H)/dH|$, is proportional to the SFD [61]. In the case of exchange-coupled systems, two DCD experiments are required to investigate the demagnetization process after field cooling: one with parallel cooling and saturating fields and one with antiparallel fields.

In Fig. 6(a) the DCD $|dM_r^{DCD}(H)/dH|$ of sample B_2 for the ZFC and FC modes are compared to investigate the effect of the metal/oxide exchange coupling. The effect of exchange coupling on the SFD is not a mere translation of the SFD towards more negative fields but it involves opposite changes in the negative and positive SF regions. The negative SFD region corresponds to antiparallel cooling and applied (demagnetization) fields, that is, to SFs for the magnetization reversal *from* the favored direction to the opposite one,

whereas the positive SFD region, where cooling and applied fields are parallel, corresponds to magnetization reversal *to* the favored direction, defined by the sign of H_{cool}. In the negative SF region, a depletion near $H = 0$ and an increased fraction of SF more negative than –1 kOe is observed. In the positive SF region, an increased fraction of SF < 1.5 kOe is observed while more positive SFs become less frequent. The effect of the exchange coupling—as revealed by the FC procedure—is to extend the distribution of negative SFs toward more negative values and to restrain positive SFs to smaller values. These changes in the SFD are the source of the shift and broadening of the hysteresis loop recorded after FC.

We carried out DCD experiments on a few samples with the main aim to show that the SFD from DCD data is equivalent to the SFD calculated by the ΔM method using the hysteresis loop data. In the latter method, SFD is approximated as $|d\Delta M(H)/dH|$, where $\Delta M(H)$ is the difference between the descending and ascending branches of the hysteresis loop. The main difference between DCD and ΔM SFDs is that in the former case M_r is truly related to the irreversible magnetization changes since it is measured at zero field, whereas ΔM is just an approximate representation of the irreversible magnetization changes [49]. The obvious advantage is that no data other than hysteresis loops are required to estimate the SFD. DCD ($|dM_r^{DCD}/dH|$) and ΔM ($|d\Delta M/dH|$) SFDs of sample B_2 for the ZFC and FC modes are compared in Figs. 6(b) and 6(c). Clearly, $|d\Delta M/dH|$ is very similar to $|dM_r^{DCD}/dH|$ and thus is an acceptable SFD; unfortunately, the former is more affected by experimental noise. The FC SFDs from ΔM data are shown in Figs. 6(d)–6(f) for selected samples, and the shape parameters of all FC SFDs can be found in [49].

The effect of varying the CoO layer thickness is very different in the two regions of the SFD. In the positive SF region, the SFD broadens with increasing t_{CoO} but its most probable SF hardly shifts and shape is not much affected. Dramatic changes are conversely observed in the negative SF region where the thicker CoO shell causes a substantial broadening and flattening of the SFD, which extends farther than –20 kOe. In order to describe the SFD shape changes, we introduce the position of the SFD peaks ($S_\pm$), corresponding to the most probable SFs, and the half-width at half-height ($B_\pm$) of the SFD peaks. The definition of $S_\pm$ and $B_\pm$ and their values for all samples can be found in [49]. In the positive SF region, S_+ and B_+ are proportional to each other, showing that the effect of t_{CoO} is a general increase of the positive SFs with minor SFD shape changes, which are confined to the small wing at high field. In the negative SF region, both S_- and B_- become more negative with increasing t_{CoO} but they are not simply related. S_- and B_- are more sensitive to t_{CoO} than S_+ and B_+. For instance, both B_+ and $B_- \cong 0.5$ kOe for sample A, but on increasing the oxide shell thickness, B_+ reaches 1.5 kOe while B_- can be as high as 4.9 kOe. In summary, the thickness of the oxide shell affects the mode and width (roughly corresponding to the EB field and coercivity, respectively) of the SFD related to the magnetization reversal from the favored FC direction to the disfavored one (negative SFs) much more than those related to the SFD for the opposite magnetization reversal.

D. Magnetic properties and oxide shell thickness

The magnetic properties of core-shell systems depend on several parameters, such as the core diameter, the shell material [62], the shell thickness [53], the AFM crystallinity [63], and the interactions with neighboring particles [64]. However, the core-shell NP films were synthesized in such a way that the NP morphology, composition, structure, crystallinity, and areal density were as constant as possible across the whole sample series, except for the thickness of the NiO and CoO layers. In the samples here investigated the formation of the NiO layer around the Ni core induces a decrease of the Ni core diameter between 2% and 7%, and it is not expected to significantly modify the magnetic properties. Therefore in the studied systems the only relevant variable parameters are the thickness of the AFM shells, including NiO, CoO, and a possible intermixed region.

The dependence of the EB effects on the thickness t_{AFM} of the AFM material is complex. For instance, the AFM anisotropy energy density can be written as $K_{AFM}\, t_{AFM}$ [62], but it would be simplistic to consider the anisotropy energy linear with respect to t_{AFM} since the AFM oxide thickness in our NPs is so small that K_{AFM} itself depends on t_{AFM}. Such a line of reasoning can be applied to other parameters such as the AFM Néel temperature, sublattice magnetization, etc. In general, a critical thickness t^* exists such that the EB vanishes for $t_{AFM} \ll t^*$ and then rapidly grows ($t_{AFM} \approx t^*$) to a constant value in the region where $t_{AFM} \gg t^*$ [7]. The investigation of the relationship between the EB effects of our thin-film assemblies of Ni/NiO/CoO core-shell NPs and the thickness of the CoO oxide layer is complicated by the presence of a thin shell of NiO intermediate between the core Ni NP and the top CoO layer. Such an intermediate layer may strongly affect the FM/AFM exchange coupling [25,65–67]. As already discussed, the magnetic properties sensitive to exchange coupling at the FM/AFM metal/oxide interface (EB field, coercivities) generally increase with the thickness of the CoO shell. Conversely, the thermal behavior of the low-field magnetization (ZFC/FC, TRM) is sensitive to neither t_{CoO} nor t_{NiO} because it is dominated by the inter-NP magnetostatic interactions, especially when H_{cool} is weak. To get some insight into the relationships between EB field, coercivities, and SFD on one hand and the thickness of the oxide layers on the other hand, we resort to linear correlation analysis, since linear effects should be prominent for such thin oxide layers. The analysis of both general trends and anomalies provided us some clues to understand the relationship between morphology and magnetism. Of course, linear correlations at most provide clues, not evidence, but correlations passing appropriate statistical tests form a reasonably sound basis to draw conclusions.

We first note that H_b, H_c, and H_{cr}^- are linearly correlated beyond a reasonable doubt while correlation with H_{cr}^+ is inferior (see Table SIII in [48]). The SFD shape parameters are correlated to H_b though to a different extent: S_-, S_+, and B_+ are moderately correlated to H_b, while B_-, the width of the SFD in the negative region, is close to exact proportionality to H_b. Thus, in what follows we can carry out correlation analysis for H_b only, knowing that similar results would be obtained for H_c, H_{cr}^-, and B_- Moreover, these strong correlations suggest that all these characteristic fields are closely related manifestations

of the FM/AFM exchange coupling and that H_b is closely related to location (H_{cr}^-) and variation (B_-) parameters of the SFD for magnetization reversal *from* the preferred direction.

Regression analysis (see Table SIV in [48]) shows that H_b has no statistically significant linear correlation with t_{NiO}, as evidenced by the failure of the statistical t and F test and the very low value coefficient of determination ($R^2 = 0.005$), meaning that just 0.5% of the variation of H_b can be attributed to the linear association with t_{NiO}. Conversely, H_b is correlated to both t_{CoO} ($R^2 = 0.45$) and $t_{NiO} + t_{CoO}$ ($R^2 = 0.57$) but the linear regression H_b vs t_{CoO} (and vs $t_{NiO} + t_{CoO}$) is of only moderate quality, mainly due to sample B_3, which lies far from the regression line. We next carried out linear regression of H_b with t_{NiO}, t_{CoO}, and $t_{NiO} + t_{CoO}$, excluding B_3 in all cases. Comparing these regressions, it is easy to see that H_b is proportional to t_{CoO}, which accounts for 97% of the variation of H_b, while t_{NiO} does not significantly account for any. (Both the t and F test fail, meaning that R^2 is not significantly different from zero.) The best-fit results are as follows:

$$H_b/\text{kOe} = (0.83 \pm 0.07)(t_{CoO}/\text{nm}), \quad R^2 = 0.970,$$
$$R = 0.985, F \text{ test}: \text{ passed}, t \text{ test}: \text{ passed}.$$

The high R^2 of the regressions without the B_3 datum shows that the EB-related parameters of sample B_3 really are anomalously large with respect to the moderate oxide shell thickness of B_3. The large slope of the regression line confirms that when a large-anisotropy oxide such as CoO is used, EB effects are larger than those observed in the NiO case (0.14 kOe/nm) [19], as already reported [62]. Moreover, it is clear that the investigated 0.7–2.7 nm t_{CoO} range lies within the EB onset region for CoO ($t_{CoO} \approx t^*$), at least when a very thin intermediate NiO shell is present.

To get more insight into the ability of t_{NiO} and t_{CoO} to account for the variation of H_b, a bivariate linear regression was carried out, $H_b = p_{NiO} t_{NiO} + p_{CoO} t_{CoO}$, either with and without the B_3 datum (see Table SV in [48]). In both cases the regression passes the F test, has $R^2 > 0.90$, and the marginal contribution of t_{NiO} in accounting for the H_b variation is not statistically significant. These results indicate that H_b is well correlated to the thickness of the CoO layer. Similar conclusions are drawn when H_{cr}^- is considered. Some insight into the anomaly of B_3 can be gained by noting that in both cases the estimated p_{CoO} is consistent with the value previously obtained by the univariate regression. This suggests that the regressor t_{NiO} has somewhat accounted for the unexpectedly large H_b and H_{cr}^- of B_3, as supported by the fact that the bivariate regressions including and excluding the B_3 datum have similar F and R^2.

Therefore, regression analysis supports the view that the EB-related parameters of sample B_3 really are anomalously large and suggests that this behavior is related to the thickness of the NiO shell. Indeed, the main difference between B_3 and the other samples is the thickness of the NiO layer: $t_{NiO}(B_3) = 0.67\,\text{nm} = 1.6$ crystal cells is not much larger than in other samples, but it is the only sample where the NiO layer is largely thicker than one crystal cell. Since it was previously found for similar Ni/NiO core-shell NPs that a significant EB field develops for $t_{NiO} \gtrsim 2\,\text{nm}$ [19], we can exclude a direct contribution of NiO to the EB field and coercivities. However, a strong enhancement of the EB effect in Co NPs dispersed in a NiO matrix was attributed to the presence of a thin CoO layer (~1 nm) between the FM NPs and the AFM matrix [25]. The AFM/AFM interaction between NiO and CoO has been studied in detail in epitaxial thin films, either repeating multilayer [65] and bilayer systems [66,67]. In all cases, it was found that NiO and CoO strongly interact by AFM/AFM exchange coupling. The layered systems have a single T_N intermediate between those of bulk NiO and CoO and are able to induce exchange bias in a soft FM top layer. In multilayers, this effect was attributed to the increase of the NiO anisotropy constant induced by CoO. Investigation of the bilayers showed that the AFM/AFM interaction depends on both NiO and CoO thickness. In particular, when $t_{CoO} = 1.5\,\text{nm}$, the AFM/AFM interaction increases up to $t_{NiO} = 2\,\text{nm}$ and then decreases for thicker NiO. In the present core-shell NPs, $t_{CoO} = 0.7$–$2.7\,\text{nm}$ and $t_{NiO} = 0.2$–$0.7\,\text{nm}$, so these findings can shed light on the behavior of our NPs. The NiO/CoO interaction produces sizeable effects in the low-T measurements but is unable to increase the overall T_N above that of CoO, probably because the NiO/CoO interface in the core-shell NPs is less crystallographically homogeneous and more defective than that of epitaxial thin films. At low T, when t_{NiO} is at least 0.7 nm thick, large effects are recorded, as previously observed [67], thus supporting the conclusion drawn on the basis of the statistical analysis that the thicker NiO layer in B_3 is related to the increased AFM/FM exchange coupling between Ni and CoO. The thicker NiO layer may favor the growth of a less defective and more homogeneous CoO layer and increase the amount of uncompensated spins (responsible for exchange bias effects), thanks to the close similarity of the crystal structure of the two oxides (lattice mismatch 2%), as recently demonstrated for Co/CoO core-shell nanoparticles embedded in a Cu_2O matrix [68]. Such structural and exchange effects may make the peaks in the ZFC/FC and TRM derivatives of sample B_3 narrower and more symmetric than those of the other samples.

V. CONCLUSIONS

Thin-film assemblies of Ni/NiO/CoO core-shell NPs have been synthesized by a three-step sequential layer deposition procedure which enables an accurate control of the NP morphology, independently for each component. STEM and SEM showed that the NPs are randomly dispersed on the substrate and HRTEM proved that the Ni core is a McKay icosahedral nanoparticle coated by a partially crystalline CoO layer. Analysis of the XPS spectra using Shard's method revealed the presence of a thin NiO shell, which STEM-EELS showed to be between the Ni core and the outer CoO layer. Investigation of the magnetic properties revealed that both exchange-coupling and magnetostatic interactions are important. The latter dominates the magnetic behavior below ~250 K, when the cooling field is absent or weak, and increases T_B to a temperature comparable to RT. Exchange coupling may contribute to this high T_B by enhancing the inter-NP magnetostatic interaction by the increase of the intra-NP anisotropy barrier. Exchange-bias effects are as strong as expected for CoO and much stronger than those of similar NPs with NiO coating. The EB field and coercivities strongly

depend on t_{CoO} in the 0.4–2.7 nm range, showing the onset of the EB in these systems. Increasing t_{CoO} leads to a large increase of the most probable, median, and the most negative switching field for the magnetization reversal *from* the favored direction determined by the cooling field to the disfavored one. The changes in SFD show up as the EB-induced hysteresis loop shift and broadening. Correlation analysis suggests that H_b and coercivities depend on t_{CoO} and not on t_{NiO} when the latter is less than 0.5 nm. However, when t_{NiO} is significantly thicker than one crystal cell, NiO strongly interacts with CoO and a dramatic boost of the EB field and coercivities ensues.

ACKNOWLEDGMENTS

This work has been supported by the Italian Ministero dell'Istruzione, dell'Università e della Ricerca through the FIRB Project, "Oxides at the Nanoscale: Multifunctionality and Applications", Grant No. RBAP115AYN. We thank one of the referees for her/his valuable and insightful comments.

[1] *Handbooks on Nanophysics: Nanoparticles and Quantum Dots*, edited by K. D. Sattler (CRC Press, Boca Raton, FL, 2011).

[2] R. Hao, R. Xing, Z. Xu, Y. Hou, S. Gao, and S. H. Sun, Synthesis, functionalization, and biomedical applications of multifunctional magnetic nanoparticles, Adv. Mater. (Weinheim, Ger.) **22**, 2729 (2010)

[3] V. Skumryev, S. Stoyanov, Y. Zhang, G. Hadjipanayis, D. Givord, and J. Nogués, Beating the superparamagnetic limit with exchange bias, Nature (London) **423**, 850 (2003).

[4] J. Nogués, V. Skumryiev, J. Sort, S. Stoyanov, and D. Givord, Shell-Driven Magnetic Stability in Core-Shell Nanoparticles, Phys. Rev. Lett. **97**, 157203 (2006).

[5] C. P. Beans and J. D Lingston, Superparamagnetism, J. Appl. Phys. **30**, S120 (1959).

[6] J. I. Martìn, J. Nogués, K. Liu, J. L. Vicent, and I. K. Schuller, Ordered magnetic nanostructures: Fabrication and properties, J. Magn. Magn. Mater. **256**, 449 (2003).

[7] J. Noguès, J. Sort, V. Langlais, V. Skumryev, S. Suriñaz, J. S. Muñoz, and M. D. Barò, Exchange bias in nanostructures, Phys. Rep. **422**, 65 (2005).

[8] T. Yamacuchu, Y. Tsukahara, T. Sakata, H. Mori, T. Yanagida, T. Kawai, and Juji Wada, Magnetic Cu–Ni (core-shell) nanoparticles in a one-pot reaction under microwave irradiation, Nanoscale **2**, 515 (2010).

[9] A. López Ortega, M. Estrader, G. Salazar-Alvarez, S. Estradé, I. V. Golosovsky, R. K. Dumas *et al.*, Strongly exchange coupled inverse ferrimagnetic soft/hard, $Mn_xFe_{3-x}O_4/Fe_xMn_{3-x}O_4$, core/shell heterostructured nanoparticles, Nanoscale **4**, 5138 (2012).

[10] C. Binns, M. T. Qureshi, D. Peddis, S. H. Baker, P. B. Howes, A. Boatwright, S. A. Cavill, S. S. Dhesi, L. Lari, R. Kroger, and S. Langridge, Exchange bias in Fe@Cr core-shell nanoparticles, Nano Lett. **13**, 3334 (2013).

[11] M. Kaur, Q. Dai, M. Bowden, M. H. Engelhard, Y. Wu, J. Tank, and Y. Qiang, Watermelon-like iron nanoparticles: Cr doping effect on magnetism and magnetization interaction reversal, Nanoscale **5**, 7872 (2013).

[12] J. B. Yi, J. Ding, Z. L. Zhao, and B. H. Liu, High coercivity and exchange coupling of Ni/NiO nanocomposite film, J. Appl. Phys. **97**, 10K306 (2005).

[13] T. Seto, H. Akinaga, F. Takano, K. Koga, T. Orii, and M. Hirasawa, Magnetic properties of monodispersed Ni/NiO core-shell nanoparticles, J. Phys. Chem. B Lett. **109**, 13403 (2005).

[14] Y. Z. Zhou, J. S. Chen, B. K. Tay, J. F. Hu, G. M. Chow, T. Liu, and P. Yang, Ni-NiO core-shell nanoclusters with cubic shape by nanocluster beam deposition, Appl. Phys. Lett. **90**, 043111 (2007).

[15] L. Del Bianco, F. Boscherini, A. L. Fiorini, M. Tamisari, F. Spizzo, M. Vittori Antisari, and E. Piscopiello, Exchange bias and structural disorder in the nanogranular Ni/NiO system produced by ball milling and hydrogen reduction, Phys. Rev. B **77**, 094408 (2008).

[16] A. C. Johnston-Peck, J. Wang, and J. B. Tracy, Synthesis and structural and magnetic characterization of Ni (core)/NiO (shell) nanoparticles, ACS Nano **3**, 1077 (2009).

[17] S. K. Sharma, J. M. Vargas, M. Knobel, K. R. Pirota, C. T. Meneses, S. Kumar, C. G. Lee, P. G. Pagliuso, and C. Rettori, Synthesis and tuning the exchange bias in Ni-NiO nanoparticulate systems, J. Appl. Phys. **107**, 09D725 (2010).

[18] S. D'Addato, M. C. Spadaro, P. Luches, V. Grillo, S. Frabboni, S. Valeri, A. M. Ferretti, E. Capetti, and A. Ponti, Controlled growth of Ni/NiO core-shell nanoparticles: Structure, morphology and tuning of magnetic properties, Appl. Surf. Sci. **306**, 2 (2014).

[19] M. C. Spadaro, S. D'Addato, P. Luches, S. Valeri, V. Grillo, E. Rotunno, M. A. Roldan, S. J. Pennycook, A. M. Ferretti, E. Capetti, and A. Ponti, Tunability of exchange bias in Ni@NiO core-shell nanoparticles obtained by sequential layer deposition, Nanotechnology **26**, 405704 (2015).

[20] M. C. Spadaro, P. Luches, F. Benedetti, S. Valeri, S. Turchini, G. Bertoni, A. M. Ferretti, E. Capetti, A. Ponti, and S. D'Addato, Investigation of Ni@CoO core-shell nanoparticle films synthesized by sequential layer deposition, Appl. Surf. Sci. **396**, 1860 (2017).

[21] A. Ceylan, A. K. Rumaiz, and S. Ismath Shah, Inert gas condensation of evaporated Ni and laser ablated CoO, J. Appl. Phys. **101**, 094302 (2007).

[22] F. T. Parker, K. Takano, and A. E. Berkowitz, Exchange coupling mechanisms at ferromagnetic/CoO interfaces, Phys. Rev. B **61**, R866 (2000).

[23] M. Gruyters, Cobalt oxide/ferromagnet bilayers: Exchange coupling and dominance of the antiferromagnet, Europhys. Lett. **64**, 803 (2003).

[24] P. Kuświk, P. L. Gastelois, M. M. Soares, H. C. N. Tolentino, M. De Santis, A. Y. Ramos, A. D. Lamirand, M. Przybylski, and J. Kirschner, Effect of CoO/Ni orthogonal exchange coupling on perpendicular anisotropy of Ni films on Pd(001), Phys. Rev. B **91**, 134413 (2015).

[25] J. A. De Toro, D. P. Marques, P. Muñiz, V. Skumryev, J. Sort, D. Givord, and J. Nogués, High Temperature Magnetic Stabilization of Cobalt Nanoparticles by an Antiferromagnetic Proximity Effect, Phys. Rev. Lett. **115**, 057201 (2015).

[26] S. D'Addato, L. Gragnaniello, S. Valeri, A. Rota, A. di Bona, F. Spizzo, T. Panozaqi, and S. F. Schifano, Morphology and

magnetic properties of size-selected Ni nanoparticle films, J. Appl. Phys. **107**, 104318 (2010).
[27] S. D'Addato, V. Grillo, S. Altieri, R. Tondi, S. Valeri, and S. Frabboni, Structure and stability of nickel-nickel oxide core-shell nanoparticles, J. Phys.: Condens. Matter **23**, 175003 (2011).
[28] S. D'Addato, V. Grillo, S. Altieri, S. Frabboni, F. Rossi, and S. Valeri, Assembly and fine analysis of Ni/MgO core/shell nanoparticles, J. Phys. Chem. C **115**, 14044 (2011).
[29] G. Bertoni and J. Verbeek, Accuracy and precision in model based EELS quantification, Ultramicroscopy **108**, 782 (2008).
[30] V. Grillo and E. Rotunno, STEM_CELL: A software tool for electron microscopy: Part I. Simulations, Ultramicroscopy **125**, 97 (2013).
[31] H. G. Schlager and H. von Löhneysen, Susceptibility of local magnetic moments in phosphorus-doped silicon near the metal-insulator transition, Europhys. Lett. **40**, 661 (1997).
[32] K. Andres, R. N. Bhatt, P. Goalwin, T. M. Rice, and R. E. Walstedt, Low-temperature magnetic susceptibility of Si:P in the nonmetallic region, Phys. Rev. B **24**, 244 (1981).
[33] A. L. Mackay, A dense non-crystallographic packing of equal spheres, Acta Cryst. **15**, 916 (1962).
[34] R. Wang, O. Dmitrieva, M. Farle, G. Dumpich, M. Acet, S. Mejia-Rosales, E. Perez-Tijerina, M. J. Yacaman, and C. Kisielowski, FePt icosahedra with magnetic cores and catalytic shells, J. Phys. Chem. C **113**, 4395 (2009).
[35] S. D'Addato, V. Grillo, A. di Bona, S. Frabboni, S. Valeri, P. Lupo, F. Casoli, and F. Albertini, Controlled co-deposition of FePt nanoparticles embedded in MgO: A detailed investigation of structure and electronic and magnetic properties, Nanotechnology **24**, 495703 (2013).
[36] D. Reinhard, B. D. Hall, P. Berthoud, S. Valkealahti, and R. Monot, Unsupported nanometer-sized copper clusters studied by electron diffraction and molecular dynamics, Phys. Rev. B **58**, 4917 (1998).
[37] C. L. Johnson, E. Snoeck, M. Ezcurdia, B. Rodrìguez-Gonzàlez, J. Pastoriza-Santos, R. M. Liz-Marzàn, and M. J. Hÿtch, Effects of elastic anisotropy on strain distributions in decahedral gold nanoparticles, Nat. Mater. **7**, 120 (2008).
[38] S. Ino, Stability of multiply-twinned particles, J. Phys. Soc. Jpn. **27**, 941 (1969).
[39] G. Rossi and R. Ferrando, Freezing of gold nanoclusters into poly-decahedral structures, Nanotechnology **18**, 225706 (2007).
[40] A. G. Shard, A straightforward method for interpreting XPS data from core-shell nanoparticles, J. Phys. Chem. C **116**, 16806 (2012).
[41] J. A. Borchers, M. J. Carey, R. W. Erwin, C. F. Majkrzak, and A. E. Berkowitz, Spatially Modulated Antiferromagnetic Order in CoO/NiO Superlattices, Phys. Rev. Lett. **70**, 1878 (1993).
[42] H. Danan, A. Herr, and A. J. P. Meyer, New determinations of the saturation magnetization of nickel and iron, J. Appl. Phys. **39**, 669 (1968).
[43] J. J. M. Franse and G. De Vries, The magnetocrystalline anisotropy energy of nickel, Physica **39**, 477 (1968).
[44] J. M. D. Coey, *Magnetism and Magnetic Materials* (Cambridge University Press, Cambridge, UK, 2010).
[45] K. Tomiyasu, T. Inami, and N. Ikeda, Magnetic structure of CoO studied by neutron and synchrotron x-ray diffraction, Phys. Rev. B **70**, 184411 (2004).
[46] P. J. van der Zaag, Y. Ijiri, J. A. Borchers, L. F. Feiner, R. M. Wolf, J. M. Gaines, R. W. Erwin, and M. A. Verheijen, Difference Between Blocking and Néel Temperatures in the Exchange Biased Fe_3O_4/CoO System, Phys. Rev. Lett. **84**, 6102 (2000).
[47] D. Givord, V. Skumryev, and J. Nogués, Exchange coupling mechanism for magnetization reversal and thermal stability of Co nanoparticles embedded in a CoO matrix, J. Magn. Magn. Mater. **294**, 111 (2005).
[48] C. Song, B. Cui, H. Y. Yu, and F. Pan, Completely inverted hysteresis loops: Inhomogeneity effects or experimental artifacts, J. Appl. Phys. **114**, 183906 (2013).
[49] See Supplemental Material at http://link.aps.org/supplemental/10.1103/PhysRevMaterials.1.036001 for the theoretical basis of the ΔM method, additional TRM data and hysteresis loops (RT and ZFC), the definitions of remanence for exchange-biased hysteresis loops, the definition and values of the shape parameters of the switching field distribution, and the linear regression analysis of EB and coercive fields.
[50] T. Bala, S. D. Bhame, P. A. Joy, B. L. V. Prasad, and M. Sastry, A facile liquid foam based synthesis of nickel nanoparticles and their subsequent conversion to $Ni_{core}Ag_{shell}$ particles: Structural characterization and investigation of magnetic properties, J. Mater. Chem. **14**, 2941 (2004).
[51] P. Zhang, F. Zuo, F. K. Urban III, A. Khabari, P. Griffiths, and A. Hosseini-Tehrani, Irreversible magnetization in nickel nanoparticles, J. Magn. Magn. Mater. **225**, 337 (2001).
[52] L. Del Bianco, A. Hernando, and D. Fiorani, in *Surface Effects in Magnetic Nanoparticles*, edited by D. Fiorani (Springer, New York, 2005).
[53] J. Nogués and I. K. Schuller, Exchange bias, J. Magn. Magn. Mater. **192**, 203 (1999).
[54] K. Takano, R. H. Kodama, A. E. Berkowitz, W. Cao, and G. Thomas, Interfacial Uncompensated Antiferromagnetic Spins: Role in Unidirectional Anisotropy in Polycrystalline $Ni_{81}Fe_{19}$/CoO Bilayers, Phys. Rev. Lett. **79**, 1130 (1997).
[55] K. J. M. Bishop, C. E. Wilmer, S. Soh, and B. A. Grzybowski, Nanoscale forces and their uses in self-assembly, Small **5**, 1600 (2009).
[56] L. Tauxe, T. A. T. Mullender, and T. Pick, Potbellies, wasp-waists, and superparamagnetism in magnetic hysteresis, J. Geophys. Res.: Solid Earth **101**, 571 (1996).
[57] D. J. Dunlop, Coercive forces and coercivity spectra of submicron magnetites, Earth Planet. Sci. Lett. **78**, 288 (1986).
[58] J.-Y. Yi, G. A. Hirata, and M. L. Rudee, Microstructure and magnetic properties of Co-CoO nanocomposite films, Mater. Res. Symp. Proc. **674**, T3.4.1 (2001).
[59] E. Menéndez, J. Demeter, J. Van Eyken, P. Nawrocki, E. Jedryka, M. Wójcik, J. F. Lopez-Barbera, J. Nogués, A. Vantomme, and K. Temst, Improving the magnetic properties of Co-CoO systems by designed oxygen implantation profiles, ACS Appl. Mater. Interfaces **5**, 4320 (2013).
[60] J. Sort, S. Suriñach, J. S. Muñoz, M. D. Baró, J. Nogués, G. Chouteau, V. Skumryev, and G. C. Hadjipanayis, Improving the energy product of hard magnetic materials, Phys. Rev. B **65**, 174420 (2002).
[61] P. I. Mayo, K. O'Grady, R. W. Chantrell, J. A. Cambridge, I. L. Sanders, T. Yogi, and J. K. Howard, Magnetic measurement of interaction effects in CoNiCr and CoPtCr thin film media, J. Magn. Magn. Mater. **95**, 109 (1991).

[62] M. S. Lund, W. A. A. Macedo, Kai Liu, J. Nogués, Ivan K. Schuller, and C. Leighton, Effect of anisotropy on the critical antiferromagnet thickness in exchange-biased bilayers, Phys. Rev. B **66**, 054422 (2002).

[63] G. C. Lavorato, E. Lima Jr., H. E. Troiani, R. D. Zysler, and E. L. Winkler, Exchange-coupling in thermal annealed bimagnetic core/shell nanoparticles, J. Alloys Compd. **633**, 333 (2015)

[64] C. Portemont, R. Morel, A. Brenac, and L. Notin, Exchange bias between cobalt clusters and oxide thin films, J. Appl. Phys. **100**, 033907 (2006).

[65] M. J. Carey, A. E. Berkowitz, J. A. Borchers, and R. W. Erwin, Strong interlayer coupling in CoO/NiO antiferromagnetic superlattices, Phys. Rev. B **47**, 9952 (1993).

[66] J. Zhu, Q. Li, J. X. Li, Z. Ding, J. H. Liang, X. Xiao, Y. M. Luo, C. Y. Hua, H.-J. Lin, T. W. Pi, Z. Hu, C. Won, and Y. Z. Wu, Antiferromagnetic spin reorientation transition in epitaxial NiO/CoO/MgO(001) systems, Phys. Rev. B **90**, 054403 (2014).

[67] Q. Li, J. H. Liang, Y. M. Luo, Z. Ding, T. Gu, Z. Hu, C. Y. Hua, H.-J. Lin, T. W. Pi, S. P. Kang, C. Won, and Y. Z. Wu, Antiferromagnetic proximity effect in epitaxial CoO/NiO/MgO(001) systems, Sci. Rep. **6**, 22355 (2016).

[68] J. A. González, J. P. Andrés, R. López Antón, J. A. De Toro, P. S. Normile, P. Muñiz, J. M. Riveiro, and J. Nogués, Maximizing exchange bias in Co/CoO core/shell nanoparticles by lattice matching between the shell and the embedding matrix, Chem. Mater. **29**, 5200 (2017).